

A Band Dispersion Mechanism for Pt Alloy Compositional Tuning of Linear Bound CO Stretching Frequencies

Nicholas Dimakis,[†] Hakim Iddir,[‡] Robert R. Díaz-Morales,[§] Renxuan Liu,^{||} Grant Bunker,[⊥] Eun-Hyuk Chung,[#] and Eugene S. Smotkin^{*,§,||}

Department of Physics and Geology, University of Texas-Pan American, Edinburg, Texas 78541,

Department of Physics, University of Illinois at Chicago, Chicago, Illinois 60607-7059, Department of

Chemistry, University of Puerto Rico at Rio Piedras, San Juan, Puerto Rico 00931, NuVant Systems, Inc.,

Chicago, Illinois 60616, Physics Division, Illinois Institute of Technology, Chicago, Illinois 60616, and

Department of Chemical Engineering, Illinois Institute of Technology, Chicago, Illinois 60616

Received: August 14, 2004; In Final Form: November 4, 2004

The C–O stretching frequency (ν_{CO}) of atop CO/Pt in PtRu alloys is compositionally tuned in proportion to the Pt mole percent. The application of a Blyholder–Bagus type mechanism (i.e., increased back-donation from the metal d-band to the hybridized $2\pi^*$ CO molecular orbitals (MOs)) to compositional tuning has been paradoxical because (1) a Pt–C bond contraction, expected with increased back-donation as the Pt mole percent is reduced, is not observed (i.e., calculated Pt–C bond is either elongated or insensitive to alloying and the binding energies of CO/Pt decrease with alloying) and (2) the lowering d-band center and increased d-band vacancies upon alloying (suggesting less back-donation to the higher energy metal hybridized $2\pi^*$ CO MOs) must be reconciled with the alloy-induced red shift of the ν_{CO} . A library of spin-optimized Pt and Pt alloy clusters was the basis of density functional theory (DFT) calculations of CO binding energies, ν_{CO} values, shifts, and broadening of $5\sigma/2\pi^*$ CO MO upon hybridization with the alloy orbitals and a DFT derived Mulliken electron population analysis. The DFT results, combined with FEFF8 local density of states (LDOS) calculations, validate a 5σ donation– $2\pi^*$ back-donation mechanism, reconciling the direction of alloy compositional tuning with the lowering of the d-band center and increased vacancies. Although the d-band center decreases in energy with alloying, an asymmetric increase in the dispersion of the d-band is accompanied by an upshift of the metal cluster HOMO level. Concomitantly, the hybridization and renormalization of the CO $5\sigma/2\pi^*$ states results in a broadening of the $5\sigma/2\pi^*$ manifold with additional lower energy states closer to the upshifted (with respect to the pure Pt cluster) HOMO of the alloy cluster. The dispersion toward higher energies of the alloy d-density of states results in more $5\sigma/2\pi^*$ CO filled states (i.e., enhanced $2\pi^*$ -back-donation). Finally, Mulliken and FEFF8 electron population analysis shows that the increase of the average d-band vacancies upon alloying and additional $2\pi^*$ back-donation are not mutually exclusive. The d-electron density of the CO-adsorbed Pt atom increases with alloying while the average d-electron density throughout the cluster is reduced. The localized electron density is manifested as an electrostatic wall effect, preventing the Pt–C bond contractions expected with increased back-donation to the $2\pi^*$ CO MOs.

Introduction

The state-of-the-art reformat/air¹ polymer electrolyte fuel cell anode catalyst is carbon-supported nanostructured PtRu (PtRu/C).^{2–5} The requirement for high dispersion restricts preparation of PtRu/C to low-temperature kinetically controlled methods that typically result in uncontrolled phase segregation, with Pt and Ru unpredictably distributed. The surface of the Pt enriched face-centered cubic (fcc) alloy (one phase among amorphous and crystalline phases)⁶ must activate the hydrogen oxidation reaction (HOR) in the presence of adsorbed CO (CO_{ads}). Potential-dependent Pt L_{III}-edge and Ru K-edge X-ray absorption near-edge spectroscopy (XANES) of PtRu/C anodes in an

operating reformat-air fuel cell showed evidence of only fully metallic Pt and Ru at practical fuel cell potentials.^{7,8} The Pt L_{III}-edge white line confirms increased d-band vacancies in the alloy.^{7,9} X-ray photoelectron spectroscopy (XPS) of arc-melted alloys and Ru modified Pt surfaces showed that the reducing environment at the fuel cell anode maintains the alloying components in a metallic state.^{10,11} Two theories on alloy enhancement of the HOR reaction are (1) CO_{ads} is not oxidized, but reduction of the CO binding energy (E_{ads}) results in more available sites for the HOR reaction, and (2) CO_{ads} oxidation is catalyzed on mixed metal catalysts, increasing HOR sites. Understanding the relative importance of these theories requires elucidation of the effects of alloying on the electronic structure of mixed metal catalysts and the interaction of alloy modified bands with the molecular orbitals of CO_{ads}.

Although electrocatalysis is a surface phenomenon, the band structure, governed primarily by the core atoms of the nanostructured catalyst (e.g., >3–5 nm), plays an important role, often referred to as a “ligand effect”.¹² We probed the effect of

* To whom all correspondence should be addressed. E-mail: esmotkin@cnetnet.upr.edu.

[†] University of Texas-Pan American.

[‡] University of Illinois at Chicago.

[§] University of Puerto Rico.

^{||} NuVant Systems.

[⊥] Physics Division, Illinois Institute of Technology.

[#] Department of Chemical Engineering, Illinois Institute of Technology.

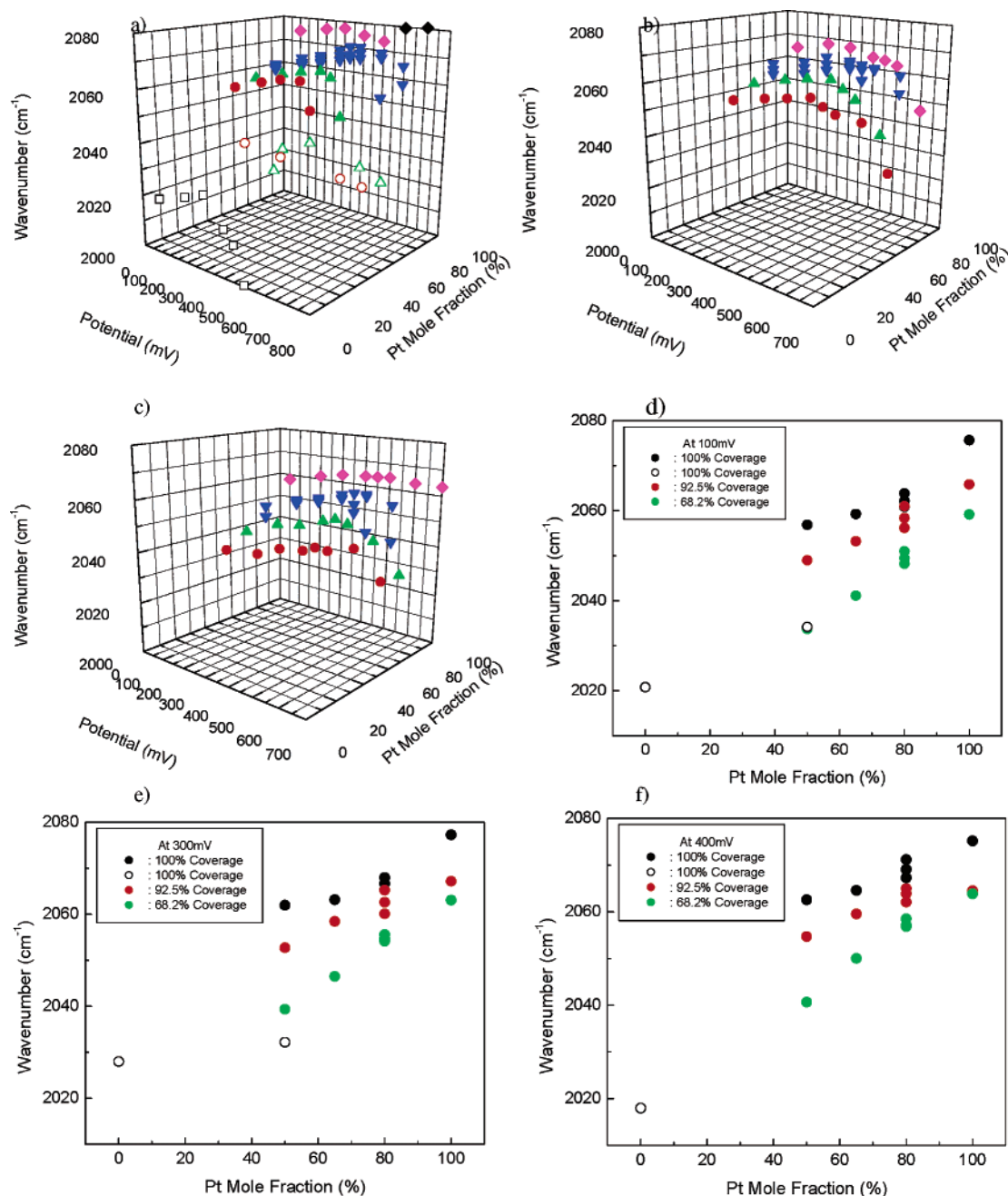


Figure 1. Electrochemically determined CO coverage, arc-melted alloy composition, and electrode potential dependence of the CO_{ads} stretching frequency: (a) 50% CO, coverage = 100%; (b) 1% CO, coverage = 92.5%; (c) 0.1% CO, coverage = 68.2%; potential dependence (versus dynamic hydrogen electrode) of CO_{ads} stretching frequency versus Pt mole fraction at (d) 100 mV, (e) 300 mV, and (f) 400 mV.

alloying on electronic structure variations with polarization modulated infrared absorption spectroscopy (PM-IRAS) of CO_{ads} . The ν_{CO} peaks obtained from a potential- and coverage-dependent PM-IRAS study of arc-melted Pt, Ru, PtRu, PtOs, and PtRuOs electrodes in aqueous acid are summarized in Figure 1a–f, showing the separated effects of coverage, alloy composition, and electrode potential.¹⁰ For any selected alloy composition, the ν_{CO} decreases as the coverage is reduced (Figure 1a–c). The open black squares of Figure 1a show that CO_{ads} is only weakly adsorbed on pure Ru in the aqueous phase and thus only observed at high coverage. The 65% and 50% Pt alloys show a high-frequency and a low-frequency manifold of ν_{CO} values at the highest coverage (Figure 1a, open green triangles and open red circles). The lower frequency species correspond to more tenaciously adsorbed bridge-bonded CO_{ads} ; the peak intensities did not diminish, as did the higher frequency peaks

when CO_{ads} oxidation commenced. The two solid black triangles correspond to very weak intensity peaks that persisted after CO_{ads} oxidation commenced on pure Pt. CO_{ads} oxidation was most facile on the hexagonal close-packed pure Ru arc-melted electrode. This study focuses on the linear bound CO on Pt. Figure 1d–f shows the compositional tuning of the ν_{CO} at constant coverage or potential: The ν_{CO} decreases in proportion to the Pt mole fraction. The ν_{CO} depends on interrelated effects including coverage related CO–CO interactions, surface and bulk catalyst composition, and solvent and surface potential effects. This work strives to factor decompose the effects of potential, CO coverage, and compositional tuning of ν_{CO} .

Blyholder^{13,14} and later Bagus and Pacchioni¹⁵ discussed the reduction of ν_{CO} when free CO is adsorbed on Pt by considering 5σ donation from the CO into the metal and back-donation from the d-band into the $2\pi^*$ molecular orbital of CO. Invoking a

Blyholder–Bagus mechanism (BBM) to the Figure 1d–f data would suggest that alloying with Ru increases back-donation to the $2\pi^*$ molecular orbital of CO, consequently reducing ν_{CO} . The dilemma is that the BBM would predict a contraction of the C–Pt bond and in increase of E_{ads} . In fact, the E_{ads} is reduced upon alloying.¹⁶ Calculated values of ν_{CO} on PtRu alloys, by Koper¹⁷ and Liao,¹⁸ were insensitive to the Pt–C bond lengths suggesting that the manifestation of orbital overlap effects on 5σ donation and $2\pi^*$ back-donation are decoupled by some other effect. The increase in d-band vacancies upon alloying, evidenced by XANES, is also difficult to reconcile with the BBM demand for increased back-donation from the metal d-bands to the $2\pi^*$ CO MOs.

Self-consistent field (SCF) methods including semi-empirical,^{19–22} Hartree–Fock,^{23,24} and DFT (cluster^{25–28} and periodic^{16,17,29–31}) are applicable to this problem. DFT under nonlocal spin approximations estimates the ν_{CO} with higher accuracy than other SCF methods.³² This study correlates our FTIR data¹⁰ with a DFT analysis of the chemisorption of CO on pure Pt and PtRu alloy clusters coupled with FEFF8³³ calculations. To ensure that reasonable cluster sizes were selected for generality of the DFT trends, a library of spin-optimized one-, two-, and three-layer clusters were examined to show convergence of the calculated ν_{CO} values to a precision of within a few percent. The trend analysis for this study required advances on the precision of calculated values more so than improvements in absolute accuracy: The benchmark average, of calculated values of this study, is sufficiently close to the measured ν_{CO} values. Spin-optimized cluster calculations have been reported by Illas et al.,²³ comparing singlet versus triplet spin configuration of a two-layer four-atom Pt cluster with CO attached to the single Pt atom in the top layer, $(\text{Pt}_3)(\text{Pt}_1)\text{CO}$. Nonspin-optimized single-cluster calculations were performed by Watwe et al.²⁵ on a three-layer Pt_{10} cluster, $(\text{Pt}_1)(\text{Pt}_3)(\text{Pt}_6)$, where all metal atoms were fixed at their crystallographic positions. Two cluster calculations have been reported by Wasileski et al.²⁶ using $(\text{Pt}_3)(\text{Pt}_3)(\text{Pt}_7)$ and $(\text{Pt}_6)(\text{Pt}_6)-(\text{Pt}_{13})$ to describe the effects of an external electric field on CO adsorption. Three cluster calculations have been reported by García-Hernández et al.²⁸ using $(\text{Pt}_3)(\text{Pt}_1)$, $(\text{Pt}_3)(\text{Pt}_7)$, and $(\text{Pt}_3)(\text{Pt}_3)(\text{Pt}_7)$ clusters. Calculations on $(\text{Pt}_3)(\text{Pt}_3)(\text{Pt}_7)$ have been also reported by Illas et al.²⁴ Calculations of C–O and C–Pt bond lengths, the binding energy of CO to Pt, and the CO_{ads} stretching frequency for various nonspin-optimized, 10-atom pure Pt and Pt based bimetallic alloy clusters have been reported by Liao et al.¹⁸ Illas et al.²³ were the first to discuss the importance of spin multiplicity in cluster calculations pertaining to CO_{ads} . Calculated ν_{CO} values in this work vary as much as 50 cm^{-1} depending on the cluster multiplicity, confirming the need for spin optimization when doing cluster calculations. Kua and Goddard performed spin-optimization when studying transition states involved with methanol oxidation on single-layer model metal surfaces.³⁴ In practice, performing a series of SCF conformational energy calculations for various multiplicities is a strategy for identification of the optimal cluster ground-state multiplicity. Table 1 show that the optimal ground-state multiplicity calculated in this study is often higher than the triplet state.

Although small cluster calculations (2–10 atoms) have the advantage of eliminating typical convergence problems of SCF or geometry optimizations, the larger clusters are more realistic models for CO adsorption on bulk surfaces and have greater potential for providing cluster-size independent CO_{ads} properties along with detailed investigations of the effect of each metal

TABLE 1: DFT Calculated HOMO, LUMO, Fermi Energies and Spin Multiplicities for a Pair of One-, Two-, and Three-Layer Pt Clusters and the Optimal Alloy Cluster^a

cluster	multiplicity	E_{HOMO} (eV)	E_{LUMO} (eV)	E_{Fermi}^b (eV)
Pt_{13}CO	7	−5.927	−5.430	−5.678
Pt_{25}CO	17	−5.903	−5.366	−5.634
$(\text{Pt}_{12})(\text{Pt}_{13})\text{CO}$	7	−5.463	−4.805	−5.134
$(\text{Pt}_{12})(\text{Pt}_{25})\text{CO}$	25	−5.540	−4.715	−5.127
$(\text{Pt}_1)(\text{Pt}_{12})(\text{Pt}_9)\text{CO}$	7	−5.531	−4.596	−5.063
$(\text{Pt}_1)(\text{Pt}_{12})(\text{Pt}_{13})\text{CO}$	9	−5.478	−4.397	−4.937
$(\text{Pt}_1)(\text{Pt}_{12})(\text{Ru}_4\text{Pt}_9)\text{CO}$	17	−5.356	−4.524	−4.940

^a The Pt_{21}CO has been omitted. ^b The Fermi energy is defined as $E_{\text{Fermi}} = E_{\text{LUMO}} + (E_{\text{HOMO}} - E_{\text{LUMO}})/2$.

layer on the ν_{CO} . The cluster-size (spin-optimized) dependence of ν_{CO} was examined (up to 37 atoms) to identify a series of Pt clusters for systematic study of alloying effects on CO_{ads} properties. Valence-electron population analysis is performed using the Mulliken population analysis technique that explicitly shows the number of electrons for each particular atomic orbital. Another approach toward examining the electron population information before and after alloying is XANES spectra on the Pt L-edge calculated by the FEFF8 program.³³ XANES-calculated L-edges through the “white line” provide insights concerning vacancies on the 4p (L_{-1}), 4d (L_{-II}), and 5d (L_{-III}) states or orbitals that have similar orbital symmetry. In addition, FEFF8 is used to determine electron densities and the atomic contribution of the local density of states (LDOS). Using experimental atomic positions, FEFF8 calculations can be used to cross-check DFT–Mulliken calculated properties. Although experimental XANES typically probes the bulk electronics of Pt and PtRu alloy catalysts, simulated XANES spectra can also be used to study both bulk electronics as well as model surface structures. These analyses can estimate the changes in electron occupancy before and after alloying thus providing a more comprehensive model of the metal/alloy CO chemisorption process.

Computational Strategy

DFT^{35–37} using the hybrid B3LYP³⁸ functional was used to determine SCF conformational energies, optimal geometries, Mulliken³⁹ orbital population analysis, and C–O stretching frequency (ν_{CO}). The B3LYP exchange–correlation functional consists of the exact Hartree–Fock and Slater local exchange functional,⁴⁰ Becke’s 1988 nonlocal gradient correction⁴¹ for the exchange with the correlation functionals of Vosko–Wilk–Nusair (VWN),⁴² and Lee–Yang–Parr (LYP).⁴³ The basis set for these calculations of Pt and Ru heavy atoms is the LACVP** which includes valence and outermost core electrons.⁴⁴ The $5s^25p^65d^96s^1$ and $4s^24p^64d^75s^1$ “valence”⁴⁵ configurations are used for Pt and Ru, respectively, while the remaining core electrons are treated with effective core potentials that account for the mass–velocity and relativistic effects. For carbon and oxygen, the 6-31G** Pople basis set⁴⁶ with all electrons being treated explicitly is used.

Jaguar 4.1⁴⁷ was used on a multiprocessor ORIGIN 2400 Silicon Graphics Server with 8 RISC12000 CPUs and 512 MB of RAM memory for each CPU node (1 node = 2 R12000). Although there are many commercial DFT codes, Jaguar incorporates the pseudospectral method^{48–53} to calculate most of the fundamental time-consuming integrals with the same accuracy as the fully analytical DFT codes. CO molecular orbitals (MOs) were visualized by correlating their corresponding energies using Molden.⁵⁴

All clusters were constructed with an fcc lattice parameter of 3.92 Å with the Pt (100) face used as the adsorbing surface. Alloys were constructed by substituting Ru atoms at nearest neighbor sites on the CO adsorbing face without changing the lattice parameter. For each cluster, the ground-state multiplicity is iteratively determined as discussed previously. The spin-optimized cluster is then geometrically optimized by letting the C, O, and adsorbing Pt atoms freely move while all other atoms remain locked in their initial positions. This prevents gross cluster relaxation, which would not be characteristic of the periodic lattice structure we aim to model. Computing the ν_{CO} using the partial Hessian approach for C, O, and the adsorbing Pt conserves CPU time avoiding the unnecessary calculation of cluster Pt–Pt normal mode vibrations.

XANES^{55,56} absorption spectra at Pt L_I, L_{II}, and L_{III} edges, electron densities (for the central absorbing Pt, the remaining scattering Pt, C, and O atoms), and the atomic contribution of the LDOS for pure Pt and PtRu alloy clusters were computed using SCF FEFF⁸³³ program. The amplitude of the resultant scattering wave includes a term in the form of $e^{-2R/\lambda}$ where λ is the photoelectron mean free path length and R is the distance of the particular scattering path. The exponential term coupled with a short core-hole lifetime limits X-ray absorption fine structure (XAFS) information on electronic and structural properties to a confined region about the central absorbing atom. A three-layer cluster arrangement is used for FEFF8 calculations with 5 atoms on the bottom layer, 12 in the middle layer, and 13 on the top layer (Pt₅, Pt₁₂, Pt₁₃) for both pure Pt and PtRu alloys. The benefit of larger clusters for XANES simulations is diminished because of the scattering wave XAFS amplitude form and core lifetimes. Alloys are modeled by incorporating Ru atoms into the cluster in the same arrangement as was used in the DFT calculations. The XANES region is well approximated by FEFF8 because of inclusion of SCF-type potentials that are necessary to simulate the near-edge region with high accuracy. Although FEFF8 SCF potentials are an improvement over previous FEFF versions, SCF DFT potentials are still a better approach over the corresponding SCF FEFF8 potentials. The ultimate approach would be the use of a hybrid DFT/FEFF for the XANES and extended X-ray absorption fine structure (EXAFS) region of the spectrum. The Debye–Waller factor (DWF), a parameter in the XAFS $\chi(k)$ equation, is an exponential of the form $e^{-2k^2\sigma^2}$ where σ^2 is the mean square variation of the particular scattering path. The DWF affects the resultant amplitude of the backscattered wave. Geometries involving wide-angle double scattering,⁵⁷ even at the low-energy range of the EXAFS and XANES, are very sensitive to the DWF. In our case, 90° multiple-scattering paths are involved, with respect to the central Pt atom; thus, all DWFs are included in the simulated FEFF calculations. These parameters are calculated by FEFF8 using the correlated Debye model for all single- and multiple-scattering paths around the absorbing Pt atom⁵⁸ using the Debye temperature (240 K for metallic Pt). Although this one-parameter Debye model for description of multiple-scattering paths has significant limitations,^{59,60} absence of the DWFs in the XAFS spectra will lead to grossly misleading results in the XANES region as explained above. A more accurate picture would result from implementation of SCF-DFT calculated DWFs for infinite lattices such as Pt and alloys.

Results and Discussion

Cluster Size (Spin-Optimized) Effects on CO Adsorption (Pure Pt). *Single-Layer Cluster Library.* A library of single-layer clusters was built by symmetrically adding Pt atoms to a

TABLE 2: Calculated C–Pt ($R_{\text{C-Pt}}$) and C–O Interatomic Distances ($R_{\text{C-O}}$), C–O Stretching Frequency ($\nu_{\text{C-O}}$), and Adsorption Energy (E_{ads}) for a Variety of Different Pure Pt and PtRu Clusters

cluster	$R_{\text{C-Pt}}$ (Å)	$R_{\text{C-O}}$ (Å)	$\nu_{\text{C-O}}$ (cm ⁻¹)	E_{ads} (eV)
Pt ₅ CO	1.801	1.151	2148	
Pt ₉ CO	1.806	1.147	2166	
Pt ₁₃ CO	1.821	1.145	2175	1.80
Ru ₄ Pt ₉ CO	1.828	1.151^a	2108	1.00
Pt ₂₁ CO	1.808	1.147	2166	
Pt ₂₅ CO	1.815	1.145	2175	1.81
Ru ₄ Pt ₂₁ CO	1.813	1.153	2113	a
(Pt ₄)(Pt ₉)CO	1.847	1.150	2131	
(Pt ₄)(Pt ₁₃)CO	1.846	1.150	2129	
(Pt ₁₂)(Pt ₉)CO	1.829	1.152	2125	
(Pt ₁₂)(Pt ₁₃)CO	1.836	1.151	2121	
(Pt ₁₂)(Pt ₂₅)CO	1.847	1.151	2124	
(Pt ₁)(Pt ₄)(Pt ₉)CO	1.827	1.148	2149	
(Pt ₅)(Pt ₄)(Pt ₉)CO	1.823	1.149	2151	
(Pt ₁)(Pt ₁₂)(Pt ₉)CO	1.827	1.151	2132	
(Pt ₁)(Pt ₁₂)(Pt ₁₃)CO	1.824	1.152	2131	2.05
(Pt ₁)(Pt ₁₂)(Ru ₄ Pt ₉)CO	1.839	1.155	2102	1.60

^a Was not calculated because of poor convergence during conformational energy calculations.

five-atom Pt (100) single layer with a CO symmetrically atop on the surface. With the exception of Pt₂₁CO, all single-layer cluster calculations converged easily. Pt₂₁CO required time-consuming fully analytical DFT calculations (non-pseudospectral method). Table 2 presents calculated C–Pt and C–O interatomic distances, C–O stretching frequencies, and binding energies of CO on Pt for all clusters of this study. There was no difference in the calculated ν_{CO} between Pt₁₃CO and Pt₂₅CO single-layer clusters, but the change in the interatomic C–Pt distance was 0.006 Å. This small change suggests that the spin-optimized 13- and 25-atom single-layer clusters are a good series to study for size and alloying effects.

Two-Layer Cluster Library. Pt atoms were overlaid upon Pt₉CO, Pt₁₃CO, and Pt₂₅CO single layers. The single-layer cluster data suggests that a five-atom base layer system is inadequate; therefore, no further studies were performed on the five-atom base layer system. A 21-atom first-layer arrangement was excluded because of convergence difficulties. Two-layer structures were systematically enlarged up to the (Pt₁₂)(Pt₂₅)CO with 25 atoms overlaid upon a 12-atom base layer configuration. The (Pt₁₂)(Pt₁₃)CO and (Pt₁₂)(Pt₂₅)CO clusters have ν_{CO} that differ by 3 cm⁻¹ and their C–Pt bonds differ by 0.012 Å. Thus, (Pt₁₂)(Pt₁₃)CO is a sufficiently large cluster to examine the effect of Ru substitution in spin-optimized two-layer clusters.

Three-Layer Cluster Library. (Pt₁)(Pt₄)(Pt₉)CO and (Pt₅)(Pt₄)(Pt₉)CO three-layer clusters were constructed by overlaying Pt atoms upon the same base bilayer. The difference in the ν_{CO} resulting from the addition of a single Pt atom on the third layer versus five Pt atoms on the third layer was 2 cm⁻¹. No difference was observed for the C–O distance whereas C–Pt distance differed by 0.004 Å. Next, using a single atom on the third layer, the first and second layers are varied as (Pt₁)(Pt₁₂)(Pt₉)CO, (Pt₁)(Pt₁₂)(Pt₁₃)CO, and (Pt₁)(Pt₄)(Pt₁₃)CO. The (Pt₁)(Pt₄)(Pt₁₃)CO system had severe SCF convergence problems.

The library calculations show sufficiently high precision that convergence of the stretching frequency values to within a few percent (wavenumber convergence) is used as a criterion for down selection to the Pt clusters to be subjected to Ru substitution for the alloy calculations. For example, the differ-

TABLE 3: Most Significant CO Molecular Orbitals for Pt₁₃CO, Pt₂₆CO, Pt₂₂Ru₄CO, and Free CO as Calculated by Jaguar and Visualized by Molden

cluster CO freq/cm ⁻¹	Pt ₁₃ CO 2175	(Pt ₁)(Pt ₁₂)(Pt ₁₃)CO 2131	(Pt ₁)(Pt ₁₂)(Ru ₄ Pt ₉)CO 2102	free CO 2211
CO orbitals	energy (eV)			
3σ	-32.350	-31.524	-31.755	-31.50
4σ	-17.555	-16.757	-17.118	-15.488
5σ	-14.938	-14.277	-14.536	-10.090 ^a
1π	-13.930 ^c	-13.133 ^c	-13.45 ^c	-18.231 ^c
5σ-s	-6.519	-12.700	-12.44	
		-10.541	-10.606	
		-9.00 ^c	-8.94 ^c	
5σ-d	-8.081	-8.690	-8.754	
	-6.969	-8.450 ^c	-8.650, -8.40	
		-8.138 ^c	-8.40, 8.00	
		-5.90 ^c	-5.80 ^c	
	-6.976 ^d , -6.833 ^d		-7.50 ^d	
2π*-d	-10.228 ^c	-11.578 ^c	-11.436 ^c	-0.5774 ^b
		-10.729 ^c	-10.740 ^c	
2π*-p	-9.553, -8.8710	-10.078 ^c	-10.057 ^c	
2π*-d	-8.870 ^c	-9.072 ^c	-9.047 ^c	
		-8.680	-8.623	
	-7.681 ^c	-8.408 ^c	-8.367 ^c	
2π*-d	-6.547 ^c	-7.246 ^c	7.200 ^c	
2π*-p	-6.976	-7.380	-7.271	
		-5.880	-5.964, -5.371	

^a HOMO. ^b LUMO. ^c Degenerate energy level. ^d Partially empty.

ence between the calculated ν_{CO} for the 22 atom three-layer cluster and the 25 atom three-layer cluster is only two wavenumbers. Similar high precision is noted for the two-layer clusters as well. Spin optimization of each cluster enabled such high precision wavenumber convergence.

Cluster Down Selection. On the basis of wavenumber convergences for C–O and C–Pt bond length calculations on the libraries of one-, two-, and three-layer clusters, the (Pt₁)(Pt₁₂)(Pt₁₃)CO system was selected as the optimal DFT cluster to be studied in a series of clusters for pure Pt and alloy calculations. The calculated ν_{CO} for (Pt₁)(Pt₁₂)(Pt₁₃)CO is 2131 cm⁻¹ (10 wavenumbers greater than the corresponding (Pt₁₂)(Pt₁₃) case) corresponding to C–O and C–Pt bond lengths of 1.152 and 1.824 Å, respectively. The effects of the spin multiplicity and HOMO and LUMO energies on various Pt clusters are summarized in Table 1. The optimal spin increases with the number of Pt atoms for the same layer configurations. The calculated Fermi energy for the optimal cluster is -5 eV, about 0.5 eV higher than that reported for bulk Pt by Skriver,⁶¹ suggesting that the adsorbed CO is primarily an electron donor to the metal lattice. DFT, depending on the particular functional and basis set used, generally overestimates normal-mode frequencies. For B3LYP and 6-31G** basis set, normal-mode frequencies are typically scaled by 0.96 (i.e., the optimal cluster scaled frequency is 2046 cm⁻¹).⁶²

Dependence of CO MOs on Cluster Structure (Pure Pt). Table 3 summarizes the splitting (i.e., broadening) and energy shifts of the free CO MOs when adsorbed upon the single-layer Pt₁₃CO and the optimal DFT cluster (Pt₁)(Pt₁₂)(Pt₁₃)CO. A progressive examination of this renormalization process by first examining the Pt₁₃CO cluster followed by the (Pt₁)(Pt₁₂)(Pt₁₃)CO cluster provides insights on the underpinning arguments behind the dependence of the ν_{CO} on cluster size. (The other CO orbitals, 3σ, 4σ, and 1π remain almost in the same position regardless of the crystal material.) The free-CO stretching frequency drops from 2211 to 2175 cm⁻¹ when symmetrically adsorbed upon a single-layer 13-atom Pt cluster. Two observed correlations are (1) the empty 2π* is now partially filled and coupled with the d/p-states of the Pt cluster and (2) the lone

pair 5σ orbital drops in energy, with the lowest energy state at -14.948 eV versus -10.090 eV for free CO, and then couples with the s/d-states of the cluster. The hybridization of the 5σ/2π* CO MOs results in partially populating the new hybrid 2π* orbital (i.e., increased back-donation) thus lowering the ν_{CO} . When the cluster size is increased from 13 to 26 Pt atoms, it is observed that (1) all hybrid 2π* orbitals are shifted to lower energies and are broadened and (2) the 5σ-s is also broadened into a band about 3.7 eV wide and the upper energy edge of the manifold is about 3.6 eV lower in energy than the discreet value associated with the Pt 13-atom layer. These effects further enhance hybridization of the 5σ/2π* CO MOs leading to increased back-donation that causes red shifting of the ν_{CO} . The C–Pt distance of the larger versus the smaller cluster is elongated by about 0.002 Å. Although this is acceptable with the hybridization scheme described above, it at first seems inconsistent with the BBM since back-donation to the 2π* antibonding orbital is bonding between the C and Pt. While this is a small change, the fact that a more substantial change toward shorter distances was not observed might be rationalized by the presence of the wall effect^{23,24} (electrostatic and Pauli repulsion), which prevents CO_{ads} from closer approach to the Pt surface because of electrostatic repulsion between the core orbitals of CO_{ads} and the cluster. This will be further elaborated on in the Mulliken population analysis in the alloy section.

Alloying Effects on CO Adsorption (PtRu). Ru is smaller than Pt and miscible up to 60 mol % with Pt. Incorporation of Ru into Pt yields fcc structures with lattice parameters decreasing as expected from Vegard's law.⁶ Although these lattice parameter changes can affect surface structure, consideration of these changes would require much larger clusters (to fabricate disordered alloy fcc lattices). Inadequate CPU speeds restrict us to alloys produced by atomic substitution of Ru atoms at unperturbed Pt positions and freezing these sites during geometry optimization. Access to faster CPUs will permit others to consider relaxation effects in realistically sized clusters in the future.

Three alloy clusters were down selected from the library of clusters studied on the basis of wavenumber convergence of

the Pt clusters: the single-layer $\text{Ru}_4\text{Pt}_9\text{CO}$ and $\text{Ru}_4\text{Pt}_{21}\text{CO}$ clusters and a three-layer $(\text{Pt}_1)(\text{Pt}_{12})(\text{Ru}_4\text{Pt}_9)\text{CO}$ cluster. The ν_{CO} for $\text{Ru}_4\text{Pt}_9\text{CO}$ cluster is reduced relative to the Pt_{13}CO cluster by 67 cm^{-1} concomitant with an increase in the calculated C—O interatomic distance by 0.006 \AA . Given the precision of the results demonstrated in Table 2, these changes are meaningful. Similarly, the ν_{CO} for $\text{Ru}_4\text{Pt}_{21}\text{CO}$ reported at 2113 cm^{-1} corresponds to a reduction of 61 cm^{-1} relative to Pt_{25}CO with an increase in the C—O bond length by 0.008 \AA . E_{ads} for the Pt_{25} cluster was not obtained because of convergence problems. The ν_{CO} for the three-layer alloy cluster $(\text{Pt}_1)(\text{Pt}_{12})(\text{Ru}_4\text{Pt}_9)\text{CO}$ is 29 cm^{-1} lower than the calculated ν_{CO} for the $(\text{Pt}_1)(\text{Pt}_{12})-(\text{Pt}_{13})\text{CO}$ three-layer cluster. The decrease in the ν_{CO} is accompanied by an increase of the C—Pt bond distance.

Binding Energies for CO—Pt/Alloy Clusters. The last column of Table 2 shows cluster E_{ads} values. Excellent agreement was obtained for the single-layer Pt_{13} and Pt_{25} clusters with values of 1.80 and 1.81 eV , respectively. The E_{ads} for single-layer Ru_4Pt_9 was calculated to be 1.0 eV . Because of poor SCF convergence, the E_{ads} for $\text{Ru}_4\text{Pt}_{21}\text{CO}$ was not obtained. Nevertheless, it is clear that alloying reduces the E_{ads} of CO on single-layer clusters. The calculated CO binding energy for the optimal three-layer $(\text{Pt}_1)(\text{Pt}_{12})(\text{Pt}_{13})\text{CO}$ cluster is 2.05 eV . This is in the range of the latest experimental value of $1.89 \pm 0.20\text{ eV}$ reported by Yeo et al.⁶³ for pure Pt at (111) face and low CO surface coverage. When the optimal Pt cluster is alloyed as $(\text{Pt}_1)(\text{Pt}_{12})(\text{Ru}_4\text{Pt}_9)\text{CO}$, the E_{ads} is reduced to 1.60 eV , the Pt—C bond is elongated, and the calculated ν_{CO} is reduced by 29 cm^{-1} . The reduction of ν_{CO} is consistent with the data of Figure 1. However, it is curious that the reduction of the C—O bond order was not accompanied by a contraction of the C—Pt bond. This will be discussed later.

Dependence of CO MOs on Alloy Structure. Table 3 summarizes the splitting and energy shifts of the optimal three-layer $(\text{Pt}_1)(\text{Pt}_{12})(\text{Pt}_{13})\text{CO}$ cluster and its analogue $(\text{Pt}_1)(\text{Pt}_{12})-(\text{Ru}_4\text{Pt}_9)\text{CO}$. Table 1 shows that the Fermi levels for the 26-atom Pt and Pt alloy clusters are essentially the same, -4.937 eV and -4.940 eV , respectively. Thus, direct comparison of energy state values using Table 3 values is justified. A band gap for the 26-atom clusters is expected for these quantum-sized clusters. Identification of the energy shifts of the hybridized $5\sigma/2\pi^*$ CO MOs when coupled with s/d/p bands of the cluster is difficult, especially close to the HOMO level, because of the extensive number and broadening of these orbitals for clusters of this size. However, it is clear that hybrid $5\sigma/2\pi^*$ CO MOs distant from the HOMO level are not subject to significant energy shifts upon alloying. Two new orbitals appear in the alloy spectrum, a partially filled 5σ -d state at -7.50 eV and a filled $2\pi^*$ -p at -5.371 eV . These are very close to the alloy cluster HOMO level. The enhanced broadening of the occupied and partially occupied hybrid $5\sigma/2\pi^*$ CO MOs increases back-bonding to the CO_{ads} and shifts the ν_{CO} to lower wavenumbers. This cause and effect relationship will be more apparent upon examination of changes in the center of the d-band LDOS of the central Pt atom and the asymmetric broadening of the band upon alloying. A band dispersion, rather than d-band center argument, will evolve from the FEFF8 calculations to be discussed later.

Mulliken Population Analysis. The observed downshift of the ν_{CO} when Pt is alloyed with Ru will be further correlated with the enhanced broadening of the hybrid $5\sigma/2\pi^*$ CO_{ads} MOs by electron density analysis of Pt atoms in the alloy clusters. Mulliken electron population analysis is used to examine variations of the $6s/5d$ electron density Pt states after atomic

TABLE 4: DFT Calculated Mulliken Electron Population for Pt_{13}CO and $\text{Pt}_9\text{Ru}_4\text{CO}$ Clusters. Spin Multiplicities (2S+1) are 7 and 25 for the Two Clusters, Respectively, and Correspond to Optimal Spin Multiplicities that Lead to the Most Probable Ground state

atoms	valence electron configuration	
	Pt_{13}CO	$\text{Ru}_4\text{Pt}_9\text{CO}$
O	$2s^{1.70}2p^{4.66}3d^{0.02}$	$2s^{1.70}2p^{4.69}3d^{0.02}$
C	$2s^{1.13}2p^{2.23}3s^{0.02}3p^{0.03}3d^{0.01}$	$2s^{1.29}2p^{2.21}3s^{0.04}3p^{0.03}3d^{0.01}$
Pt	$6s^{0.83}5d^{8.98}6p^{0.04}6d^{0.02}7p^{0.01}$	$6s^{0.96}5d^{9.19}6p^{0.09}6d^{0.01}7p^{0.01}$
Pt/Ru	$6s^{1.10}5d^{9.11}6p^{0.02}6d^{0.01}$	$5s^{0.83}4d^{6.72}5p^{0.05}5d^{0.01}6p^{0.01}$
Pt	$6s^{0.70}5d^{9.19}6p^{0.01}$	$6s^{1.07}5d^{9.09}6p^{0.02}$
Pt	$6s^{0.71}5d^{9.22}$	$6s^{1.15}5d^{8.99}$

substitution of Pt with Ru atoms. Table 4 shows Mulliken population analysis for single-layer Pt_{13}CO and $\text{Ru}_4\text{Pt}_9\text{CO}$ clusters. Replacement of selected Pt atoms with Ru causes (1) an increased 5d-orbital electron density for the adsorbing Pt atom along with a decrease in the corresponding orbital electron density population for the remaining Pt atoms in the cluster and (2) all Pt atoms exhibit increased 6s electron density population.

The effect of alloying on the electron density of the Pt $6s/5d$ orbitals can be somewhat separated from the effect of CO chemisorption by focusing attention on the Pt atoms away from the CO adsorption region (distant Pt atoms). The $6s$ -orbital population of distant Pt atoms increases because of electron transfer from the $5d$ state. This explains the increase in d-band vacancies upon alloying. The effect of CO chemisorption is analyzed by examining changes on the valence of the central adsorbing Pt atom. This atom has increased 5d-electron density upon alloying because of either (1) electron density donation from the hybrid 5σ CO MO or (2) direct donation from the Ru atoms since the 4d-electron density of the Ru in the alloy is lower than expected from isolated Ru atoms (the valence electronic configuration for Ru atoms is $4d^75s^1$). Although Mulliken population analysis is not free of artifacts, the trends observed are generally reliable and thus can provide valuable information about charge transfer within the model cluster.⁶⁴ Further increasing the cluster size by adding more Pt atoms causes an increase in the 5d occupancy of these additional Pt atoms without affecting the population of the previous Pt atoms in the cluster. This is consistent with the ligand effect¹² (i.e., the modification of the adsorptive properties of a given site via electronic effects by the neighbors), rather than a limitation of Mulliken population technique. In summary, the Mulliken population analysis suggests that the average number of d-band vacancies is increased in a local region about the CO_{ads} .

The DFT calculations show that Ru alloying does not contract the C—Pt distances: They remain the same or, in the largest cluster, are elongated. The Mulliken population analysis shows that when Pt is alloyed with Ru, the electron density of the C $2s$ orbital increases. The increased C $2s$ electron density together with an increase in the Pt $6s$ electron density may lead to an electrostatic repulsion between the Pt and the C atoms, that is, an electrostatic wall that prevents C—Pt bond contraction. Inadequate CPU speeds limit us to basis sets that use effective core potentials when heavy atoms such as Pt and Ru are included in the calculations, precluding the study of the core electron configuration of the metal atoms and consequently the acquiring of computational data that may explicitly determine the existence of electron densities relevant to an electrostatic repulsion effect that prevents the decrease of the C—Pt interatomic distance.

FEFF8 Calculations on Pure Pt and Pt—Ru Clusters. *XANES White Line.* Figure 3 shows simulated XANES spectra for Pt L-edges. The L_I, II edges (Figure 3a, b) have no white lines and therefore the atomic $5p$ and $4d$ Pt states are filled for

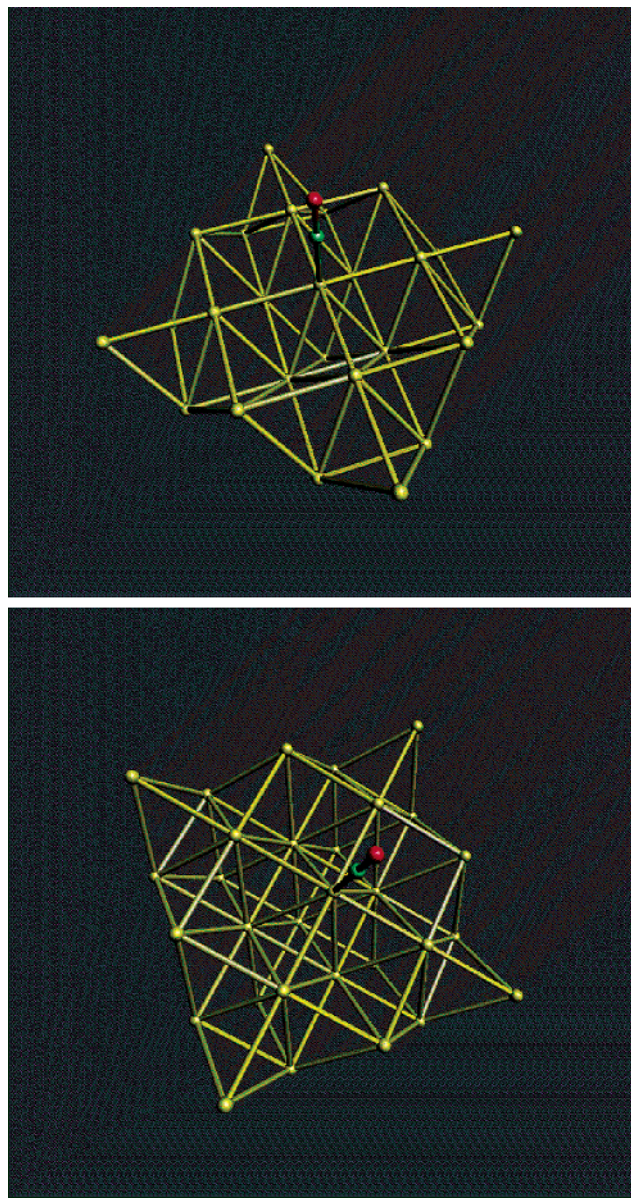


Figure 2. Optimal cluster for Pt(100) face for DFT (top) and for XANES (bottom).

both pure Pt and alloy clusters in full agreement with Mulliken–DFT population analysis presented above. Figure 3c (Pt L_{III} edge) shows that the average 5d band electron population is decreased when Pt is alloyed with Ru by atomic substitution, consistent with previously reported experimental XANES spectra.⁷

Fermi Level and Electron Densities. The Fermi level of the optimal, XANES pure Pt cluster (Figure 2, bottom) and the corresponding alloy cluster coincide at approximately -7.44 eV which allow us to compare energy levels between these two clusters. The FEFF8 calculated Fermi level appears at a lower energy value than the DFT calculated Fermi level for all clusters (approximately -4.94 eV for the optimal DFT cluster). FEFF8 calculations typically systematically shift the Fermi level by a few eV.⁶⁵ The electron density of the central active Pt atom and the average electron density over the other Pt scatterers are shown in Table 5. FEFF8 calculated electron densities correspond to the electron density of a renormalized orbital at a particular angular momentum per atomic potential (absorber, type of scatterer) whereas Mulliken population analysis denotes number of electrons per atomic state per atom (e.g., electron

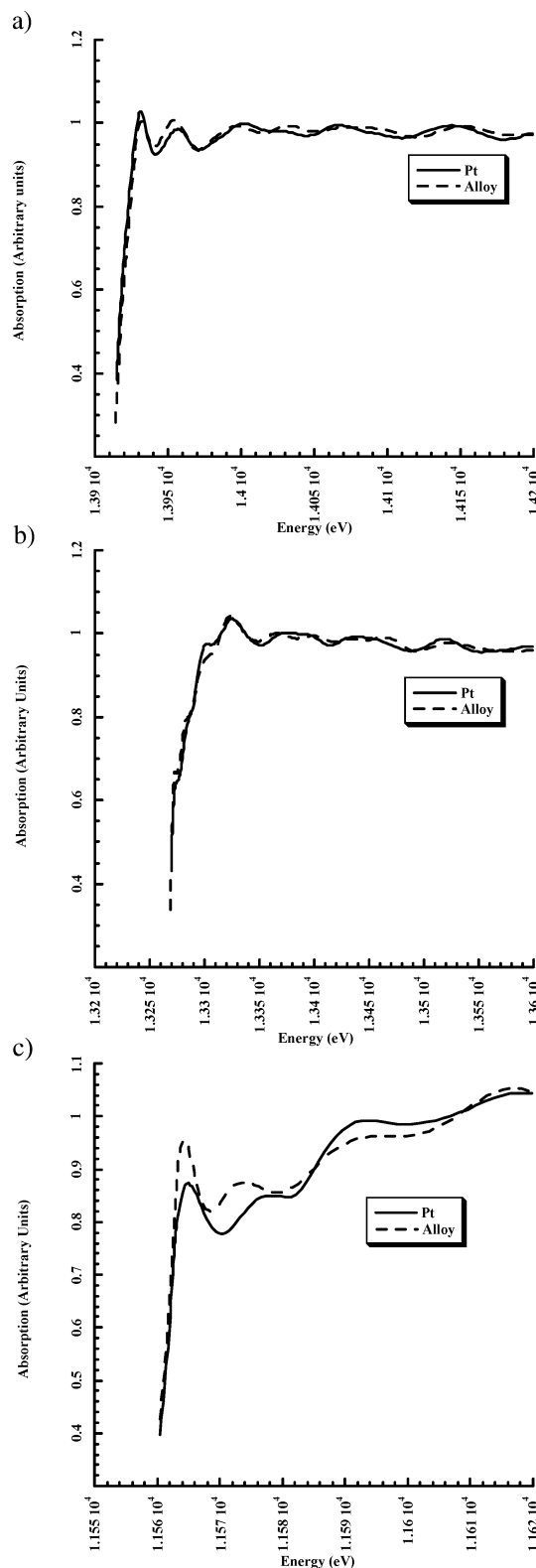


Figure 3. FEFF8 simulated XANES spectra at Pt L-edges for the optimal Pt and Pt–Ru XANES clusters: (a) L_I, (b) L_{II}, and (c) L_{III} edges.

density for the central Pt for the 5d state). This explains the presence of valence Pt p-electron type orbitals for clusters in Table 5. The FEFF8 calculations complement the Mulliken population analysis fully elucidating the mechanism for creation of d-band vacancies when Pt is alloyed with Ru: Electrons are transferred from the d-band to the s- and p-bands of the cluster thus reducing the d-electron density of all atoms of the PtRu

TABLE 5: FEFF8 Calculated Electron Densities for Pure Pt and Alloy Cluster (Pt₅(Pt₁₂)(Pt₁₃) with and without CO

cluster	atoms	pure Pt	alloy
Pt ₅ Pt ₁₂ Pt ₁₃	absorbing Pt	s ^{0.808} _p ^{0.706} _d ^{9.189} _f ^{0.140}	s ^{0.865} _p ^{0.793} _d ^{9.175} _f ^{0.142}
	scatterer Pt	s ^{0.792} _p ^{0.682} _d ^{8.385} _f ^{0.147}	s ^{0.761} _p ^{0.763} _d ^{8.298} _f ^{0.165}
Pt ₅ Pt ₁₂ Pt ₁₃ CO	absorbing Pt	s ^{0.795} _p ^{0.736} _d ^{8.952} _f ^{0.136}	s ^{0.712} _p ^{0.758} _d ^{8.946} _f ^{0.202}
	scatterer Pt	s ^{0.790} _p ^{0.703} _d ^{8.380} _f ^{0.147}	s ^{0.765} _p ^{0.772} _d ^{8.305} _f ^{0.164}
	O	s ^{1.848} _p ^{4.033} _d ^{0.199}	s ^{1.770} _p ^{4.065} _d ^{0.153}
	C	s ^{1.258} _p ^{2.111} _d ^{0.356}	s ^{1.291} _p ^{2.056} _d ^{0.436}

cluster with the exception of the Pt central absorber as will be discussed below. Although the Mulliken population analysis shows transfer to the s-band, it provides no information concerning the p band. The FEFF8 calculations complete the mechanistic model by inclusion of the p band effects. When CO is adsorbed on a central Pt atom, the renormalized Pt d-orbital overlaps and envelops the C and O atoms as seen from Table 5. Thus, the electron density of this orbital is equal to the sum of the d-electron densities of the Pt, C, and O atom. The increased d-density of the CO adsorbing Pt atom upon alloying (9.508 for pure Pt vs 9.538 for alloy cluster) is consistent with DFT derived Mulliken population. Thus, two completely independent methods of analysis point to an increase of the electron density in the hybrid CO $2\pi^*$ upon alloying. In the absence of CO, the alloying of Pt with Ru causes the X-ray absorber Pt s-electron density to increase along with a decrease of the s-electron density for the scattering Pt atoms. However, the adsorption of CO causes a decrease of the adsorbing Pt atom s-electron density along with an increase of the adsorbing and scattering Pt atoms p-electron density.

Atomic Contribution of the Local Density of States (LDOS). The atomic contribution of the LDOS for both the adsorbing and the scattering Pt atoms are shown in Figure 4. The energy axis has been offset to coincide the FEFF8 with the DFT calculated Fermi level. The solid lines correspond to the absorber Pt atom while the dotted correspond to the scatterers. Narrowing of the central absorber d-LDOS relative to the d-LDOS for the scattering Pt atoms is due to the formation of a core hole at the central absorbing atom. Alloying Pt with Ru causes the center

of the d-LDOS of all Pt atoms to shift to lower energies. Adsorption of a single CO molecule to the absorbing Pt atom causes a further lowering of the d-LDOS center along with broadening, while the corresponding d-LDOS of the Pt scatterer atoms are not significantly affected by CO chemisorption. This is true for both pure Pt and alloy clusters. The DFT calculations show that upon alloying, additional hybrid $5\sigma/2\pi^*$ CO states appear in the energy spectrum and the entire $5\sigma/2\pi^*$ band is upshifted in energy (i.e., the HOMO is shifted to a higher energy value, Table 3). A lowering of the d-band center concomitant with an upshift of the $5\sigma/2\pi^*$ band might suggest diminished back-donation from the d-band to the CO $2\pi^*$ components of the hybridized orbitals. However, a closer examination of the d-LDOS (Figure 4 inset) reveals that alloying results in asymmetric broadening of the absorber Pt d-band with a greater number of filled states at the high-energy side. Hammer et al.⁶⁶ have shown the importance of consideration of the dispersion of bands as well as the center of the d-band. The reconciliation of the Figure 1 FTIR data (compositional tuning) with the computational results is not possible without consideration of the alloy-induced band dispersion. Consistent with DFT calculations (Table 3), these additional hybrid CO MOs that are on the surface of the d-LDOS of the central absorber Pt will be contributing to more back-bonding to the CO. This effect causes more mixing of the hybridized $5\sigma/2\pi^*$ CO MOs as confirmed by DFT.

This first analysis of the alloy compositional tuning of the ν_{CO} of atop CO_{ads} on Pt(alloys) shows that back-donation increases when Ru is alloyed into Pt. The lack of C–Pt bond contraction is due to a wall effect augmented by increased C 2s electron density upon alloying. Orbital overlap contributions are the key factor in explaining compositional tuning of the ν_{CO} on Pt in PtRu alloys, with a wall effect responsible for the reduced binding energies. However, it is important not to over generalize our results. Consider the work of Koper where the potential energy surface for CO_{ads} has been elegantly factor decomposed into steric (electrostatic and Pauli repulsion) and orbital overlap contributions, the latter of which is further

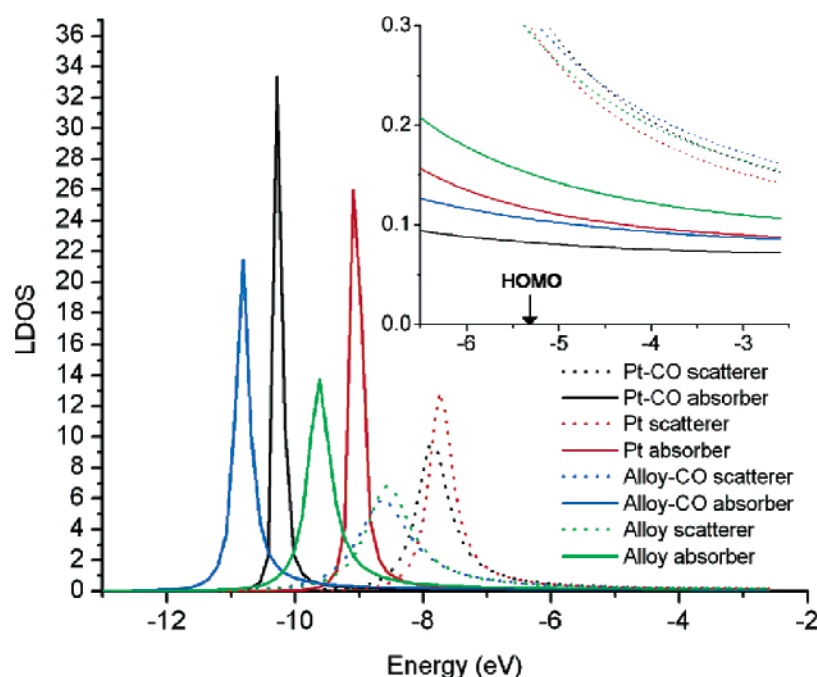


Figure 4. FEFF8 calculated atomic contribution of the LDOS for the optimal Pt and Pt–Ru XANES clusters, with and without CO. As Pt is alloyed, more filled $5\sigma/2\pi^*$ hybrid CO MOs appear close to the HOMO.

decomposed into 5σ donation and back-donation to the CO $2\pi^*$.⁶⁷ Koper shows that the substantial difference between the ν_{CO} on Pt versus the ν_{CO} on Ru is due almost entirely to steric factors rather than to orbital overlap considerations. Koper's comparison of CO/Pt to CO/Ru, though not directly analogous to our comparison of CO/Pt(Pt) to CO/Pt(PtRu), illustrates that orbital overlap does not always dominate ν_{CO} tuning, particularly when the tuning involves change of the adsorbing atom.

Our conclusion, drawn from an admittedly simple cluster model that increased band dispersion leads to increased $2\pi^*$ back-donation, is not necessarily in conflict with the Knight shift and relaxation observations of Pt/Ru and PtRu–CO high surface area samples.⁶⁸ Our calculations also suggest weaker Pt–C bonding with alloying.

Conclusion

The PM-IRAS of linear bound CO/Pt on Pt and Pt alloyed with Ru and Os shows compositional tuning where the ν_{CO} of CO_{ads} decreases as the Pt mole fraction is decreased. Application of a Blyholder–Bagus back-donation mechanism (BBM) to explain compositional tuning has been paradoxical because a predicted contraction of the Pt–C bond and increase of the E_{abs} is not substantiated by DFT: E_{abs} decreases with alloying. The calculated elongation of the Pt–C bond is consistent with calculated reductions of CO E_{abs} upon alloying. The calculated d-band center shifts to lower energies, in the wrong direction if back-bonding to the higher energy hybridized/renormalized $2\pi^*$ CO orbitals is to be invoked without consideration of changes in the dispersion of the band upon alloying.

The compositional tuning trends are explained by a computational approach, integrating FEFF8 and DFT calculations (including Mulliken population analysis) with our previous experimental XANES and potential-dependent CO_{ads} PM-IRAS. Precise (on the basis of ν_{CO} convergence) calculations were obtained by carefully selecting clusters down selected from a library of spin-optimized clusters studied by DFT.

The integrated computational approach reconciles the increase of d-band vacancies and the lowering of the d-LDOS center (when Pt is alloyed with Ru) with compositional tuning trends. Although the d-band center is lowered upon alloying, suggesting less overlap with the higher energy renormalized components of the hybridized $5\sigma/2\pi^*$ CO MOs, the increased dispersion of the d-band resulting from alloying, coupled with the broadening and lowering of the lower edge of the CO orbital manifold, actually results in more back-donation. Mulliken and FEFF8 electron density population analysis confirms that although the average d-electron density of the cluster is decreased upon alloying, the corresponding d-electron density of the central Pt atom upon which CO is adsorbed is increased, thus enhancing the CO donation–back-donation mechanism. Additionally, FEFF8 calculated d-LDOS shows that although alloying lowers the center of d-band of the absorber Pt, the band is asymmetrically broadened resulting in more $5\sigma/2\pi^*$ CO filled states.

The tuning of the ν_{CO} as the alloy Ru content is increased is a result of increased filling of renormalized hybridized $5\sigma/2\pi^*$ CO MOs consistent with a BBM mechanism. Although the d-band center shifts away from the lower edge of the higher energy CO MOs, the increased dispersion of both the d-band and the CO orbital manifold is responsible for increased back-donation that reduces the bond order between the carbon and oxygen molecule, lowering the ν_{CO} . Finally, the calculations show increased C 2s orbital density upon alloying, which may contribute to an electrostatic wall effect (i.e., stiffening of the Pt–C bond) preventing contraction of the metal–carbon bond

length. We are now in the process of obtaining soft-shell XANES of CO on alloy catalysts to experimentally quantify the distribution of electrons on CO_{ads} .

Acknowledgment. This work was funded by the ARO DURIP grant DAAD19-00-1-0095 and the NASA-UPR Center for Nanoscale Materials under NASA URC Grant #NCC3-1034.

References and Notes

- (1) Reformate hydrogen derived from the reforming of fuels such as methane, gasoline, diesel, and methanol. Reformates typically have high levels of CO.
- (2) Watanabe, M.; Uchida, M.; Motoo, S. *J. Electroanal. Chem.* **1987**, 229, 95.
- (3) Gasteiger, H. A.; Markovic, N.; Ross, P. N.; Cairns, E. J. *J. Phys. Chem.* **1994**, 98, 17.
- (4) Cameron, D. S.; Hards, G. A.; Thompson, D. In *Proceedings of the Workshop on DMFC*; Landgrebe, A. R., Sen, R. K., Wheeler, D. J., Eds.; Proceedings—Electrochemical Society, Pennington, NJ, 1992; pp 10–23.
- (5) Beden, B.; Leger, J.-M.; Lamy, C. In *Modern Aspects of Electrochemistry*; Bockris, J. O'M., Conway, B. E., White, R. E., Eds.; Plenum Press: New York, 1992; Vol. 22, pp 97–247.
- (6) Gurau, B.; Viswanathan, R.; Liu, R.; Lafrenz, T. J.; Ley, K. L.; Smotkin, E. S.; Reddington, E.; Sapienza, A.; Chan, B. C.; Sarangapani, S. *J. Phys. Chem.* **1998**, 102, 9997.
- (7) McBreen, J.; Mukerjee, S. In *Interfacial Electrochemistry: Theory, Experiment, and Applications*; Wieckowski, A., Ed.; Marcel Dekker: New York, 1999; pp 895–914.
- (8) Viswanathan, R.; Liu, R.; Smotkin, E. S. *Rev. Sci. Instrum.* **2002**, 73, 2124.
- (9) O'Grady, W. E.; Hagans, P. L.; Pandya, K. I.; Maricle, D. L. *Langmuir* **2001**, 17, 3047.
- (10) Liu, R.; Iddir, H.; Fan, Q.; Hou, G.; Bo, A.; Ley, K. L.; Smotkin, E. S.; Sung, Y.-E.; Kim, H.; Thomas, S.; Wieckowski, A. *J. Phys. Chem. B* **2000**, 104, 3518.
- (11) Kim, H.; Rabelo de Moraes, I.; Tremiliosi-Filho, G.; Haasch, R.; Wieckowski, A. *Surf. Sci.* **2001**, 474, 203.
- (12) Frelink, T. Ruthenium Promotion for the Electrochemical Oxidation of Methanol. Ph.D. Thesis, Technische University Eindhoven, The Netherlands, 1995; Chapter 9, pp 119–129.
- (13) Blyholder, G. *J. Phys. Chem.* **1964**, 68, 2772.
- (14) Blyholder assumed CO 5σ orbital to be constant.
- (15) Bagus, P. S.; Pacchioni, G. *Surf. Sci.* **1992**, 278, 427.
- (16) Hammer, B.; Morikawa, Y.; Norskov, J. K. *Phys. Rev. Lett.* **1996**, 76, 2141.
- (17) Koper, M. T. M.; Shubina, T. E.; van Santen, R. A. *J. Phys. Chem. B* **2002**, 106, 686.
- (18) Liao, M.-S.; Cabrera, C.; Ishikawa, Y. *Surf. Sci.* **2000**, 445, 267.
- (19) Anderson, A. B.; Grimes, R. W.; Hong, S. Y. *J. Phys. Chem.* **1987**, 91, 4246.
- (20) Anderson, A. B.; Grantscharova, E. *J. Phys. Chem.* **1995**, 99, 9143.
- (21) Anderson, A. B.; Ray, N. K. *J. Phys. Chem.* **1982**, 86, 4851.
- (22) Anderson, A. B.; Grantscharova, E.; Seong, S. *J. Electrochem. Soc.* **1996**, 143, 2075.
- (23) Illas, F.; Zurita, S.; Rubio, J.; Marquez, A. M. *Phys. Rev. B* **1995**, 52, 12372.
- (24) Illas, F.; Zurita, S.; Marquez, A. M.; Rubio, J. *Surf. Sci.* **1997**, 376, 279.
- (25) Watwe, R. M.; Spiewak, B. E.; Cortright, R. D.; Dumesic, J. A. *Catal. Lett.* **1998**, 51, 139.
- (26) Wasileski, S. A.; Koper, M. T.; Weaver, M. J. *J. Phys. Chem. B* **2001**, 105, 3518.
- (27) Bleakley, K.; Hu, P. *J. Am. Chem. Soc.* **1999**, 121, 7644.
- (28) Garcia-Hernandez, M.; Curulla, D.; Clotet, A.; Illas, F. *J. Chem. Phys.* **2000**, 113, 364.
- (29) Ruban, A.; Hammer, B.; Stoltze, P.; Skiver, H. L.; Norskov, J. K. *J. Mol. Catal. A* **1997**, 115, 421.
- (30) Ge, Q.; Desai, S.; Neurock, M.; Kourtakis, K. *J. Phys. Chem. B* **2001**, 105, 9533.
- (31) Shubina, T.; Koper, M. *Electrochem. Acta* **2002**, 47, 3621.
- (32) Goddard, W. A. Private Communication, California Institute of Technology, 2000.
- (33) Ankudinov, A. L.; Ravel, B.; Rehr, J. J.; Conradson, S. D. *Phys. Rev. B* **1998**, 58, 7565.
- (34) Kua, J.; Goddard, W. A. *J. Am. Chem. Soc.* **1999**, 121, 10928.
- (35) Hohenberg, P.; Kohn, W. *Phys. Rev. B* **1964**, 136, 864.
- (36) Kohn, W.; Sham, L. J. *Phys. Rev. A* **1965**, 140, 1133.
- (37) Parr, R. G.; Yang, W. *Density Functional Theory of Atoms and Molecules*; Oxford University Press: New York, 1989.

- (38) Becke, A. D. *J. Phys. Chem.* **1993**, 98, 5648.
- (39) Mulliken, R. S. *J. Chem. Phys.* **1955**, 23, 1833.
- (40) Slater, J. C. *Quantum Theory of Molecules and Solids*; McGraw-Hill: New York, 1974; Chapter 4.
- (41) Becke, A. D. *Phys. Rev. A* **1998**, 38, 3098.
- (42) Vosko, S. H.; Wilk, L.; Nusair, M. *Can. J. Phys.* **1980**, 58, 1200.
- (43) Lee, C.; Yang, W.; Parr, R. G. *Phys. Rev. B* **1998**, 37, 785.
- (44) Hay, P. J.; Wadt, W. R. *J. Chem. Phys.* **1998**, 82, 299.
- (45) Inclusion of the outermost core electrons with the valence electron is necessary because these core orbitals have similar size as the valence electrons.
- (46) Hehre, W. J.; Radom, L.; Schleyer, P. V. R.; Pople, J. A. *Ab initio Molecular Orbital Theory*; Wiley: New York, 1987.
- (47) Jaguar 4.1, Schrodinger Inc., Portland, OR.
- (48) Friesner, R. *Chem. Phys. Lett.* **1985**, 116, 39.
- (49) Friesner, R. *J. Chem. Phys.* **1987**, 86, 3522.
- (50) Friesner, R. *J. Chem. Phys.* **1986**, 85, 1462.
- (51) Ringnalda, M. N.; Won, Y.; Friesner, R. *J. Chem. Phys.* **1990**, 92, 1163.
- (52) Langlois, J.-M.; Muller, P. R.; Coley, T. R.; Goddard, W. A.; Ringnalda, M. N.; Won, Y.; Friesner, R. *J. Chem. Phys.* **1990**, 92, 7488.
- (53) Ringnalda, M. N.; Belhadj, M.; Friesner, R. *J. Chem. Phys.* **1990**, 93, 3397.
- (54) Schaftenaar, G.; Noordik, J. H. *J. Comput.-Aided Mol. Des.* **2000**, 14, 123.
- (55) Stern, E. A. In *X-ray Absorption*; Koningsberger, D. C., Prins, R., Eds.; Wiley, New York, 1988; Chapter 1.
- (56) Lee, P. A.; Pendry, B. *Phys. Rev. B* **1975**, 11, 2795.
- (57) Bouldin, C. E.; Bunker, G.; McKeown, D. A.; Forman, R. A.; Ritter, J. J. *Phys. Rev. B* **1988**, 38, 816.
- (58) The central absorbing atom Pt atom used for FEFF8 calculations is the same Pt atom that CO adsorbed. Therefore, terms Pt absorber and Pt adsorber refer to the same atom in the cluster.
- (59) Dimakis, N.; Bunker, G. *Phys. Rev. B* **1998**, 58, 2467.
- (60) Poiarkova, A. V.; Rehr, J. J. *Phys. Rev. B* **1999**, 59, 948.
- (61) Skriver, H. L.; Rosengaard, N. M. *Phys. Rev. B* **1992**, 45, 9410.
- (62) Scott, A. P.; Radom, L. *J. Phys. Chem.* **1996**, 100, 16502.
- (63) Yeo, Y. Y.; Vattuone, L.; King, D. A. *J. Chem. Phys.* **1997**, 106, 392.
- (64) Bagus, P. S.; Illas, F.; Sousa, C.; Pacchioni, G. Fundamental Material Science I. In *Electronic Properties of Solids using Cluster Methods*; Kaplan, T. A., Ed.; Plenum: New York, 1994.
- (65) Ankudinov, A. L. Private communication, University of Washington, 2003.
- (66) Hammer, B.; Nielsen, O. H.; Norskov, J. K. *Catal. Lett.* **1997**, 46, 31.
- (67) Koper, M. T.; van Santen, R. A.; Wasileski, S. A.; Weaver, M. J. *J. Chem. Phys.* **2000**, 113, 4392.
- (68) Tong, Y. Y.; Kim, H. S.; Babu, P. K.; Waszczuk, P.; Wieckowski, A.; Oldfield, E. *J. Am. Chem. Soc.* **2002**, 124, 468–473.